Materials Characterization 194 (2022) 112369

Contents lists available at ScienceDirect

Materials Characterization

journal homepage: www.elsevier.com/locate/matchar

A structure metric for quantitative assessment of fracture surfaces in 3D conceived based on confocal laser scanning microscopy data

Evgenii Vasilev [a], Jie Wang [b], Marko Knezevic [a,*]

[a] Department of Mechanical Engineering, University of New Hampshire, Durham, NH 03824, USA
[b] National Engineering Research Center of Light Alloy Net Forming, Shanghai Jiao Tong University, Shanghai 200240, China

ARTICLE INFO

Keywords:
Microstructures
Fractography
Confocal laser scanning microscopy
Structure metrics

ABSTRACT

Assessment of fracture surfaces typically involves the identification of qualitative features such as dimples, grain facets, and river patterns to determine type of fracture. The present study formulates a measure termed Real-to-Projected Area (RPA) ratio/metric to quantitatively assess fracture surfaces. Fracture surfaces of several metallic alloys tested monotonically and in fatigue to fracture including three Mg alloys, a Ti alloy in two conditions, and a Ni-based superalloy were observed using confocal laser scanning microscopy in 3D and quantitatively assessed using the metric. The metric successfully separated fracture surfaces obtained after fatigue testing from those obtained after monotonic tension testing. Specifically, the values of the metric were found to be in the range of 40–80 pct for fatigue fracture, while 90–140 pct for monotonic tension fracture. As a result, the metric can be used to distinguish between fracture in fatigue and fracture in monotonic tension when fracture types / loading modes are unknown. Moreover, the metric is sensitive to ductility of tested alloys as well as any presence of critical defects in the microstructure responsible for rapid fracture such as intermetallic inclusions. An added utility of the metric is also to identify outliers in the data such as invalid mechanical tests.

1. Introduction

Metrics for quantitative description of microstructure-property relationships are essential in the era of materials informatics and machine learning [1–10]. Numerical data and statistical correlations rather than qualitative observations are needed to formulate such metrics. Such quantitative links are being used to improve existing and develop new material models for advanced materials [11–20].

Fractography is a discipline aimed at studying fracture surfaces of materials to possibly determine cause of fracture in engineering structures. Fracture assessment is especially important in analyses of industrial failures that can lead to significant damage to property and even loss of human lives [21]. The problem is greater today than in the past because more can go wrong with always more technologically complex modern products. The information derived from in-depth fracture analyses can be valuable for offsetting some potential failures, improvement of engineering designs, and improvement of materials. By accessing fracture by fractographic examinations, weak links in the structure of a given material system can be determined and later reinforced to improve resistance to fracture of the material.

Consulting engineers are always looking into better ways to accelerate resolving various legal issues in fracture of components. Therefore, advancing fractography techniques is important to provide accurate and reliable data for such analyses [22–25].

Fractography is typically concerned to determine type of fracture – ductile or brittle, fatigue or monotonic overload. Often, it is critical to establish a type of fracture as loading mode can be unknown, for example, if an engineering part is primarily designed for fatigue loading but prematurely fractures due to some excessive overload.

As a matter of fact, in view of the complexity of the fracture surfaces the vast majority of fractographic studies are performed only qualitatively. Characteristics such as presence of dimples, grain facets, river pattern are used to characterize the type of fracture [26]. However, this approach heavily relies on the observer's subjective judgement that is not supported by quantitative parameters but rather skills and experience. Thus, an error of human judgement can naturally appear in the results.

In attempting to mitigate this problem, several quantitative parameters have been established to characterize the fracture. Among them are roughness, real fracture surface area, projected fracture surface area,

* Corresponding author at: University of New Hampshire, Department of Mechanical Engineering, 33 Academic Way, Kingsbury Hall, W119, Durham, New Hampshire 03824, United States.
E-mail address: marko.knezevic@unh.edu (M. Knezevic).

https://doi.org/10.1016/j.matchar.2022.112369
Received 16 June 2022; Received in revised form 24 August 2022; Accepted 2 October 2022
Available online 6 October 2022

facet sizes, area fractions (such as area of stable crack growth versus unstable crack growth), and spacing between various features [26], [27]. However, their explicit relation to the fracture type is often missing.

The success of fractography heavily relies on the accuracy and correctness of data acquisition. The latter can be conducted via visual inspection and instruments such as magnifying lens, optical microscopes, or scanning electron microscopes (SEM). SEM became a standard tool for routine fractography due to a wide range of magnifications, sufficient depth of field, and high resolution. Even though traditional SEM can do characterization of fracture surfaces in most of the cases, SEM provides 2D images that are used for examinations. However, fracture surfaces are fundamentally in 3D, and thus, 3D properties should be imaged for the most accurate characterization [27]. Quantification of such properties could further assist in fracture characterization by means of traditional 2D SEM and make it more reliable.

A number of 3D imaging techniques have been developed such as white light interferometry, atomic force microscopy (AFM), 3D optical microscopy [28,29], and stereo imaging in the SEM [30–33]. However, interferometry and AFM are not suitable for measurement of very rough surfaces with regions oriented at high angles that are very common in fracture surfaces. Optical 3D microscopy has limited resolution and purely relies on the software processing of local contrast that can lead to large errors in areas such as steep slopes. Stereo SEM can achieve much higher resolution but also has a number of limitations such as distortion errors and beam blockade by surfaces with large high differences [30]. These limitations prevent a wide use of this technique.

Confocal laser scanning microscopy (CLSM) is yet another technique capable of 3D reconstruction of surface topography. In contrast to digital optical 3D microscopes, where all reflected light is registered and then algorithmically stacked into 3D profile, pinhole system in CLSM allows the passage of only reflected light that lies in the focal plane. Thus, each registered image contains only focused reflection, and these reflections are used to create a "true" 3D profile thus reducing error of the reconstruction. Another advantage of CLSM is that ultraviolet laser with 405 nm wavelength can be used to achieve lateral resolution as low as 0.12 μm surpassing visible light microscopes. Although the resolution of CLSM is lower compared to SEM, it can serve as a supplement or even standalone instrument for 3D fracture surface analysis at a wide range of magnifications. CLSM does not require vacuum or conductivity of the inspected surface, costs a fraction of an SEM instrument, and requires minimal maintenance. Virtually any material can be analyzed by CLSM in a reasonably short time and at a low cost. Modern CLSM offers high automation of data acquisition and capturing detailed 3D profiles at length scales from sub-μm to a few mm. These unique capabilities have enabled a broad variety of applications in materials science. These include, but not limited to, examination of wear damage [34,35], topography of coatings [34], roughness characterization, corrosion [36,37], and fractography [36–45].

The present study is focused on the application of CLSM to fractographic analysis and quantitative characterization of fracture surfaces. Similarly to the previous work [46], where authors established a correlation between the normalized fracture surface area (Rs) and ductile/brittle fracture, in this work we introduce a Real-to-Projected Area (RPA) ratio/metric to distinguish fatigue and monotonic tension overload fracture in Mg alloys, a Ti alloy, and Ni-based superalloy. Many samples are observed under CLSM in 3D and the data used to calculate the metric values. The values are presented and insights from these discussed. Interestingly, larger differences in the metric values between fatigue and monotonic tension fracture are found for more ductile materials. Additionally, utility of the CLSM data and underlying metrics for validation of fatigue tests and detection of critical defects are discussed. Here, the metric values are shown to be sensitive to the presence of critical defects in the microstructure responsible for rapid fracture such as intermetallic inclusions.

2. Materials and experimental procedures

Six different alloys are selected for the study including an extruded Mg-1.61Y-1.16Zn, an extruded Mg-10.42Y-4.16Zn, and a rolled WE43 magnesium alloys, a Ti-6Al-4V (Ti64) titanium alloy fabricated using additive manufacturing in two different conditions (as printed and heat treated (HT)), and a wrought nickel-based superalloy, Inconel 718, (Table 1). Mg-1.61Y-1.16Zn and Mg-10.42Y-4.16Zn are alloys containing LPSO (long-period stacking order) phase in estimated quantities of 5% and 50%. Quantity of the LPSO phase is reflected in the alloy labels presented in Table 1 as Mg LPSO 5% and Mg LPSO 50%. The rest of the studied alloys are single phase. Selection of alloys was based on their attractive mechanical properties, especially for aerospace industry, and availability of samples tested under similar condition in monotonic tension, low-cycle fatigue (LCF) and high-cycle fatigue (HCF). The objective was to acquire a very comprehensive dataset using CLSM for subsequent quantitative analyses. Short labels are signed to the alloys as presented in Table 1. These labels will be used for referencing each material and/or condition later in the text.

Microstructure in alloys was characterized by optical microscopy and electron backscattered diffraction (EBSD), as presented in Fig. 1. Some of these microstructures were presented in prior works [47–56]. Optical microscopy was used for the characterization of the Mg LPSO 50% alloy because the LPSO phase cannot be indexed by means of standard EBSD analyses software. In the optical microscopy image (Fig. 1b), lighter color corresponds to α-Mg, while darker color corresponds to the LPSO phase. Inverse pole figure (IPF) triangles are provided to describe the orientation of indexed crystals relative to a selected sample axis in the EBSD scans in Fig. 1. Evidently, the studied materials have very different initial microstructures rationalizing the objective of this comprehensive study.

Mechanical testing in monotonic tension and low-cycle fatigue of the alloys was performed on a servo hydraulic MTS machine with a loading capacity of 250 kN. Samples used for tension testing were according to ASTM E8 with the gauge section of 25 mm in length and 6 mm diameter. Samples for LCF were made according to ASTM E606 and tested under symmetric tension-compression loading under controlled strain amplitude. Mechanical testing in HCF was performed using an ASTM E466–15 standard sample on an RBF-40HT rotating beam tester. Drawings of the LCF and HCF specimens are provided in the appendix. For more details on alloys, their microstructural characterization, and mechanical testing, readers are referred to [47–50,52,57,58].

In this study, we do not focus on structure-properties relationships of the materials, as the main point of the work is to determine how the proposed metric can characterize fracture surfaces of the materials with different microstructures, strength, and ductility. This can be especially important in engineering utilizing various materials, from magnesium alloys to titanium to nickel, and so on. If a single metric could be used to characterize various materials instead of developing specific metrics for specific materials, this can significantly reduce complexity of fracture assessments.

Laser confocal and optical microscopy was performed on 62 samples using a confocal laser scanning microscope Olympus OLS-5000. Data acquisition and processing were performed in Olympus Data Acquisition and Olympus Data Processing software packages. Because samples for tension/LCF and HCF had different cross-section, two different objectives were used to ensure sufficient resolution of scans and to limit number of stitched images to less than 64 (recommended by Olympus). x50 objective LMPLFLN50XLEXT was used for the HCF samples, while x10 objective MPLFLN10XLEXT was used for the tensile and LCF samples. Images were taken using violet laser in high dynamic range (HDR) mode and visible light with no HDR. The entire area of fracture surface was split into 5 × 5 to 6 × 6 areas and a 3D scan (a stack of images along Z axis) was taken at each area using laser light and visible light. Then, these 3D stacks taken at each area were stitched into a single 3D map to form an entire fracture surface per observed sample. Selected 3D maps of

Table 1
Labels, nominal chemical composition, thermomechanical treatment, elongation to fracture, ultimate tensile strength, and performed tests for alloys used in the present work.

Alloy label	Nominal composition, weight %	Thermo-mechanical treatment	Elongation to fracture, %	Ultimate tensile strength, MPa	Tests performed (number of investigated samples)	Reference
Mg LPSO 5%	Mg balance, 1.61 Y, 1.16 Zn	Extruded	17.5	290	Tension (1), LCF (5)	N/A
Mg LPSO 50%	Mg balance, 10.42 Y, 4.16 Zn	Extruded	12	360	Tension (1), LCF (5)	N/A
WE43	Mg balance, 3.7–4.3 Y, 2.4–4.4 Nd, at least 0.4 Zr	Rolled and T6 annealed	4	300	Tension (3), LCF (4), HCF (5)	[49]
Ti64 non-HT	Ti balance, 6 Al, 4 V	As additively manufactured	5	1350	Tension (3), LCF (7), HCF (6)	[50], [51]
Ti64 HT	Ti balance, 6 Al, 4 V	Additively manufactured and heat treated	9	1050	Tension (3), HCF (5)	[50], [51]
Inconel 718	55.5 Ni, 18.2 Cr, 5.5 Nb, 3.3 Mo, 1.15 Ti, 0.35 Mn, 0.35 Si, 0.3 Cu, 0.3 Al	Wrought	16.5	1570	Tension (3), LCF (5), HCF (6)	[48]

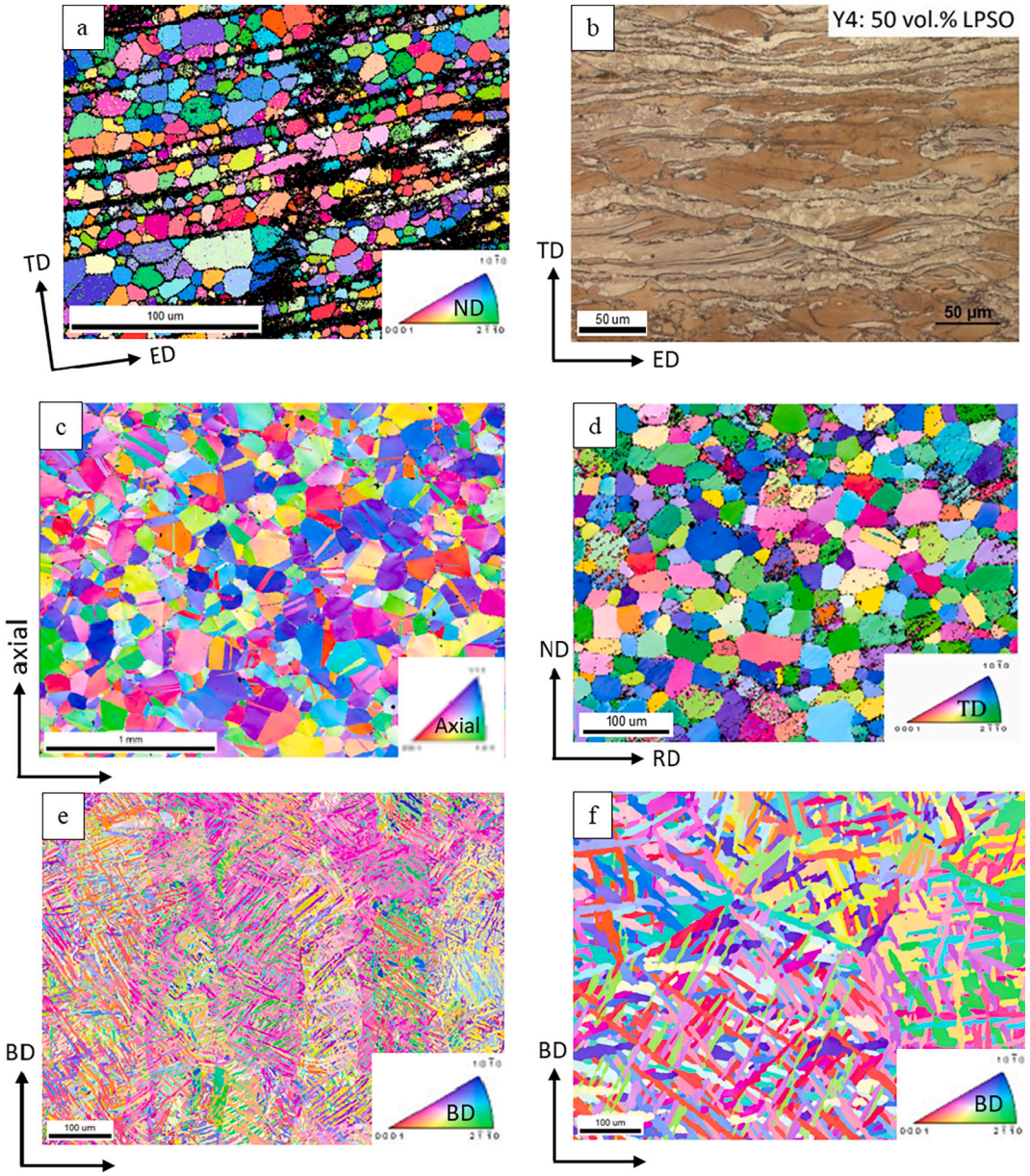

Fig. 1. Inverse pole figure (IPF) maps (a, c-f) and optical image (b) showing the initial microstructure in studied alloys: (a) Mg LPSO 5%, (b) Mg LPSO 50%, (c) Inconel 718, (d) WE43, (e) Ti64 non-HT, (f) Ti64 HT [47]–[51]. Lighter color on (b) corresponds to α-Mg and darker color corresponds to the LPSO phase. BD – build direction used in additive manufacturing; RD – rolling direction; TD – transverse direction; ND – normal direction during rolling; ED – extrusion direction; Axial – forging direction.

fracture surfaces for tested alloys are presented in the appendix.

Data processing included noise reduction (Fig. 2) by removal of points with intensity less than a threshold was performed to ensure proper identification of fracture surfaces in 3D and circular areas in 2D projections avoiding spike noise on the edges of the sample's cross-sections. To quantify roughness, an Arithmetical Mean Height (Sa) and the Real-to-Projected Area (RPA) metric were used. The latter one was inspired by the Olympus quantitative parameter Developed interfacial area ratio (Sdr). RPA is calculated for the selected area using the following formula:

$$\mathrm{RPA} = \frac{1}{A}\left[\iint_A \left(\sqrt{\left[1+\left(\frac{\partial z(x,y)}{\partial x}\right)^2+\left(\frac{\partial z(x,y)}{\partial y}\right)^2\right]}-1\right)dxdy\right] \bullet 100\%, \quad (1)$$

where A is the projected area of an analyzed surface, while x, y, z are 3D coordinates of a particular point on the analyzed fracture surface. Only data from reflected laser light were used for calculation of the height and roughness parameter. After image processing, 3 types of data are plotted in 2D and 3D: (1) intensity of the reflected visible light, (2) intensity of the reflected laser light, and (3) height maps. Different types of intensities (visible/laser) are plotted for different samples and images for best representation of structural features.

3. Results and discussion

3.1. Real-to-Projected Area (RPA) as a parameter for quantitative assessment of fracture surfaces

Topology of fracture surfaces can be described using several different quantitative measures. The most common measures involve roughness parameters. From the previous work reported in [46], it is known that ductility of fracture surfaces can be characterized using area metrics, while the roughness parameters such as Ra/Sa are less preferable because they are grain size dependent. The same work established a strong correlation between the normalized surface area and ductility (or brittleness) of fracture in a commercial hot-rolled low carbon steel, S235JR. The present work relies on the RPA measure to quantitatively assess fracture surfaces. In particular, the present work is concerned with evaluating the sensitivity of the RPA metric/ratio to monotonic tension overload, LCF at different strain amplitudes, and HCF at different stress amplitudes. Intuitively, as the level of plastic deformation possible to accumulate before ultimate fracture increases, the more developed fracture surfaces should be. As a result, values of RPA should be the lowest for HCF, increasing to LCF, and the highest for monotonic tension fracture surfaces.

Fig. 3 presents results for 62 fracture surfaces characterized by CLSM accompanied by Table 2 presenting values of Standard Deviation for tests shown on Fig. 3b. The figure shows a plot of the RPA ratio/metric for Ti64 non-HT and Mg LPSO 50% alloys tested in LCF at different strain amplitudes. The plot reveals that there is no a strong correlation between RPA and strain amplitudes in LCF for either of the two alloys. In contrast to the expectation of increasing RPA with increasing the plastic strain, some points at high strain amplitudes had lower RPA than points at lower strain amplitudes. Similarly, no appreciable correlation was also established between RPA and stress amplitudes in HCF. The spread of measured RPA values in HCF was even smaller than in LCF. The latter is illustrated in Fig. 3b, where HCF test are depicted by blue squares. From this figure, we can see that the tolerance bars (i.e. the spread of the values) are narrower for the HCF tests (blue squares) than for the LCF tests (red squares). These variations of RPA at different stress/strain amplitudes in fatigue are attributed to statistical variation in the microstructures.

Since there was no correlation established between RPA and stress/strain amplitude in fatigue, we assumed that samples of one alloy tested in LCF/HCF represent a single group of RPA values with a tolerance spread. The tolerance spread included all samples per alloy category. The approach is applicable for applications, where stress or strain in fatigue loading of parts is not precisely controlled as in labs.

From the results presented in Fig. 3b, we noticed that RPA for HCF is higher than for LCF which contrasts the expectation of higher RPA for higher plastic strain. This can be attributed to the difference in the applied loading mode and potential smearing of surfaces during testing. LCF testing was performed in tension-compression that lead to top and bottom surfaces hitting each other during testing. This interaction of top and bottom surfaces happens during the crack growth until the final rupture. HCF testing was performed using the rotating beam test (RBT) setup in which the pure bending load profile is imposed over test specimens. This load profile is different from the tension-compression one in LCF. The center of specimens is not loaded, while the surface of test specimens is at the maximum load in RBT. The LCF versus HCF tests were also performed with different sample geometries that can also affect development of fatigue cracks because of the size effect. Thus, we attribute the difference in RPA between HCF and LCF to a cumulative effect of these conditions, but, we do not attempt to separate HCF and LCF by values of RPA.

More importantly, a clear difference in RPA between fatigue (including LCF and HCF) and tension overload is observed. Based on the observations from the data for all alloys, values of RPA are established to be in a range of 40–80 pct for fatigue and 90–140 pct for tension

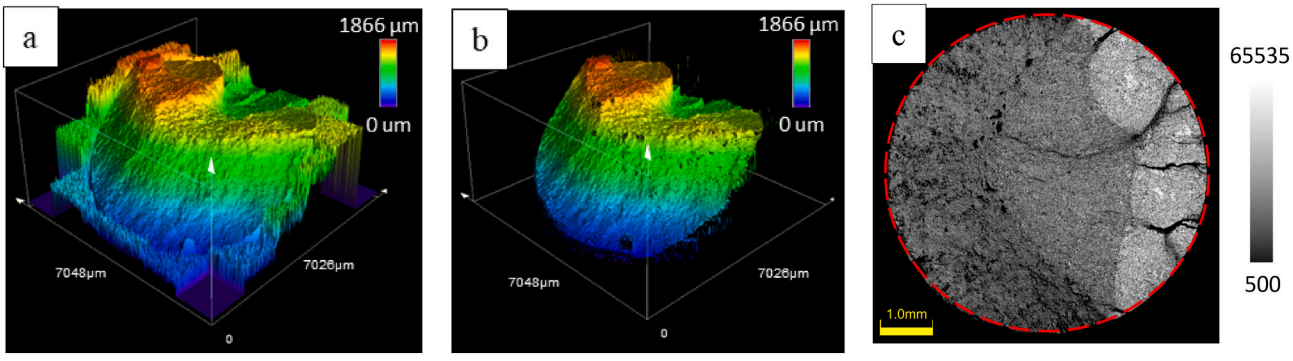

Fig. 2. Procedure for noise reduction: (a) 3D height map plotted from the as-scanned data, (b) 3D height map plotted from points with intensity greater than a selected threshold, and (c) 2D laser intensity map. Here, red dashed outline indicates the region of interest (ROI) selected for quantification. Note that the intensity scale in (c) is applicable to all subsequent images in laser and visible light. (For interpretation of the references to color in this figure legend, the reader is referred to the web version of this article.)

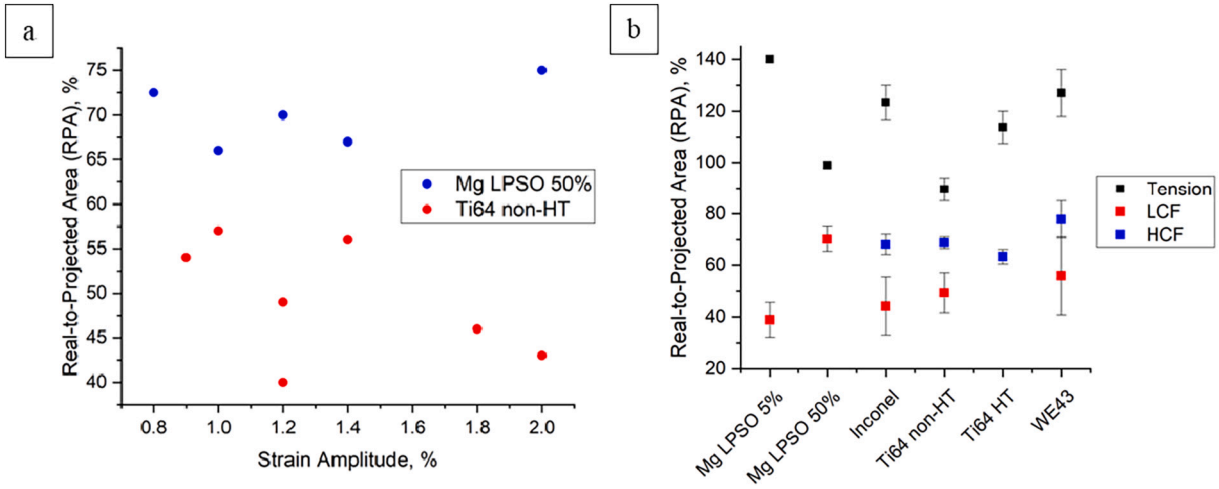

Fig. 3. Real-to-Projected Area (RPA) ratio of fracture surfaces for: (a) Ti64 non-HT and Mg LPSO 50% alloys tested in LCF at different strain amplitudes and (b) all alloys tested in tension, LCF, and HCF.

Table 2
Values of Standard Deviation for measured Real-to-Projected Area (RPA) data presented in Fig. 3b.

Material	Type of the test		
	Tension	LCF	HCF
Mg LPSO 5%	N/A	5.03	N/A
Mg LPSO 50%	N/A	3.75	N/A
WE43	8.19	10.29	5.78
Ti64 non-HT	3.91	6.63	1.51
Ti64 HT	5.51	N/A	2.17
Inconel 718	7.64	10.42	3.56

overload. Though these ranges seem to be close on the border, mean values are 60 pct and 115 pct respectfully, which is enough for the reliable quantification. The differences appear larger for more ductile materials, which have higher importance for most of structural applications, while different microstructures (Fig. 1) play a secondary role. With increasing ductility of the alloys, differences in RPA between fatigue and tension overload also increase. For example, for Ti64 non-HT (elongation to fracture 5%) this difference is 15 pct while for Ti64 HT (elongation to fracture 9%) the difference is 50 pct. Similar trend is observed for Mg LPSO 5% and Mg LPSO 50%, which have 12 and 17.5% elongation to fracture respectively, while their respective RPA ratios are 28 and 100 pct. As materials with enhanced ductility are typically preferred for most structural applications, larger differences in RPA between fatigue and tension overload make fracture assessment more reliable.

3.2. Detection of critical defects in alloys and validation of fatigue tests based on RPA

While metallurgical defects are present to a certain extent in most materials, not all of them affect mechanical characteristics in the same manner. While some defects can barely weaken the material, others can lead to crack initiation or early fracture. Thus, it is a crucial task of fractographic studies to distinguish these critical defects which drastically degrade properties of alloys and cause fracture.

Fig. 4 provides an illustration of how critical defects can be distinguished from non-critical by means of CLSM. Here, images of fracture surfaces for 3 samples are presented: (a) Mg LPSO 50% after LCF at strain amplitude 0.8%, (b) Mg LPSO 50% after LCF at strain amplitude 1.2%, (c,d) Mg LPSO 5% after LCF at strain amplitude 0.8%. Note that images on (a, d) are taken using visible light and images (b, c) are taken laser light for best representation of structural features. Blue lines on images indicate direction of crack growth, red arrows indicate inclusions, green arrows indicate crack initiation site, and red dashed line outlines a zone of stable crack growth.

On all 3 samples, there are inclusions present (marked with red arrows), however, their resultant effect is different for samples in Fig. 4a,b from that in Fig. 4c,d. For samples in Fig. 4a,b, zone of crack growth (stable and/or unstable) smoothly propagates through inclusions which look uninvolved in the acceleration of the crack growth. In contrast, for sample on Fig. 4c,d, transition from crack growth to rupture occurs along imaginary dashed red line connecting several inclusions. It becomes clear that these inclusions cause rapid rupture, so they can be defined as "critical" in this case. The 3D map in Fig. 4d better illustrates the transition from crack growth to rupture enabling more reliable identification of fracture zones and those inclusions/defects that are critical to crack propagation and rupture.

The qualitative observation is well supported by the quantitative data. For Mg LPSO 5%, typical values of RPA in LCF are 39 ± 7 pct (Fig. 3b) while for a sample with critical inclusions (Fig. 4c,d), RPA is 82 pct which is far beyond measurement tolerance for samples without critical defect.

CLSM can also help to validate fatigue tests by observing fracture morphology for subsequent quantification. Fig. 5 shows images of fracture surface of alloy Mg LPSO 50% after LCF at strain amplitudes 0.8, 1, and 1.2%. During testing, the sample in Fig. 5b experienced much more rapid fracture compared to the samples tested at similar strains (those in Fig. 5a,c), and was registered as an invalid point on a Coffin-Manson plot for the alloy [59–61]. These three samples including the "defective" one were selected for the analyses to quantify the difference in fracture morphology.

Visually, the surface of the sample tested at strain amplitude 1% looks different from samples tested at 0.8% and 1.2% strain amplitudes. An expert judgement could define the sample presented on Fig. 5b as invalid due to shiny and coarser appearance compared to the counterparts, however, this conclusion would be purely qualitative. Addition of roughness data from CLSM allows an observer to compare samples not just qualitatively but quantitatively. In a given example on Fig. 5, the sample on Fig. 5b has roughness Sa = 3.4 and RPA = 36%, while samples

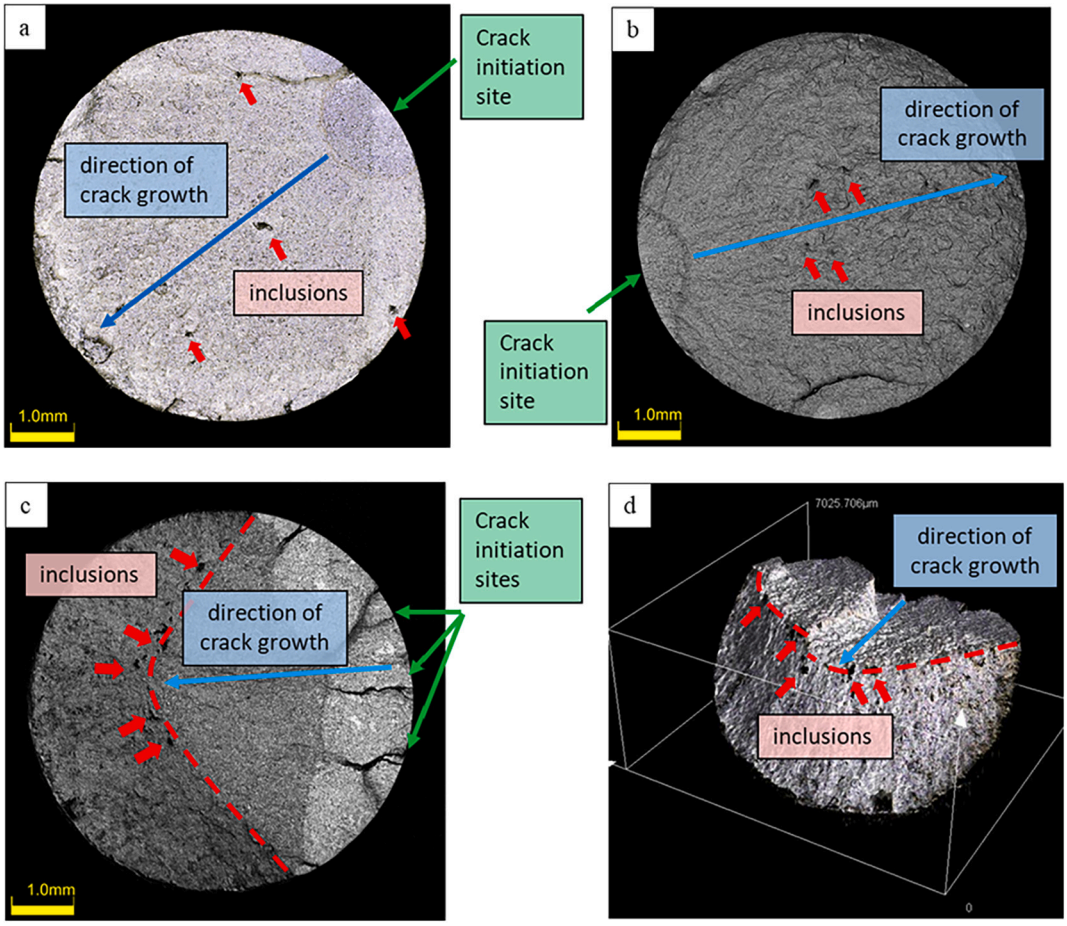

Fig. 4. Images of fracture surfaces: (a) Mg LPSO 50% after LCF at strain amplitude 0.8%, (b) Mg LPSO 50% after LCF at strain amplitude 1.2%, (c,d) Mg LPSO 5% after LCF at strain amplitude 0.8%. Images (a, d) are taken using visible light and (b, c) are taken using laser light for better representation. Blue lines indicate direction of crack growth, red arrows indicate inclusions, green arrows indicate crack initiation site, and red dashed lines outline the zone of stable crack growth. (For interpretation of the references to color in this figure legend, the reader is referred to the web version of this article.)

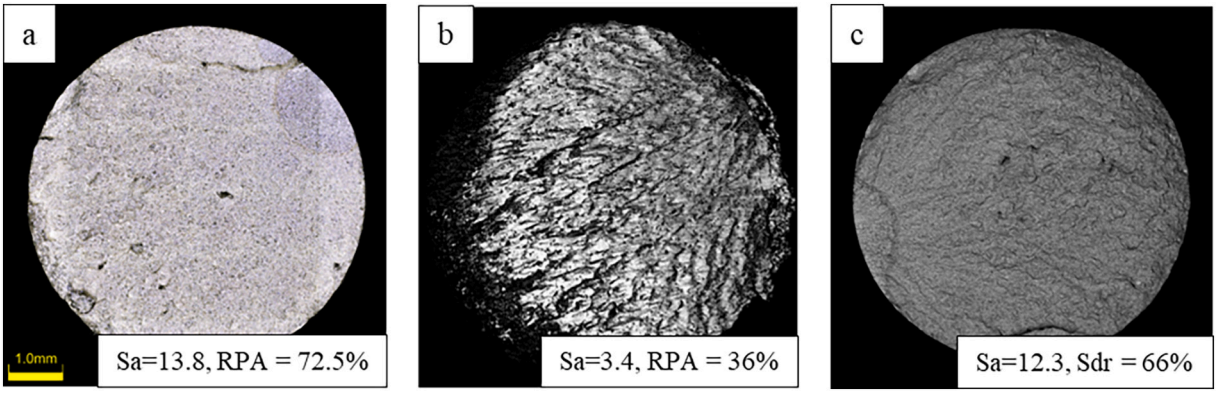

Fig. 5. Images of fracture surfaces of Mg LPSO 50% after LCF at strain amplitudes of: a) 0.8%, b) 1%, c) 1.2%. Image (a) is taken using visible light and (b, c) are taken using laser light for better representation. Difference in visual appearance of fracture surfaces on (a,c) and (b) is supported by quantitative differences in roughness parameters Sa and RPA.

on Fig. 5a,c have roughness parameters Sa = 13.8 and 12.3 respectfully, and RPA = 72.5% and 66% respectfully. In contrast to qualitative judgement of "rough" surface on Fig. 5b, roughness value is lower for this sample which signifies importance of qualitative metrics and not just qualitative observations. By comparison of these values, it becomes clear that the difference between Sa and RPA is too large to be explained by simple difference in strain amplitude, and the test resulted in fracture surface from Fig. 5b was rather invalid, which is also supported by much lower fatigue life. We remind that Fig. 3 already stated that RPA is not a strong function of strain amplitude. Thus, mechanical data and quantitative optical observations support each other, and the final judgement on the validity of the test can be made not only subjectively by observer but supported by quantitative parameters derived from CLSM. We do not further investigate what caused this early fracture in the sample on Fig. 5b, though abnormally low RPA and Sa as well as shiny appearance of the surface can potentially indicate embrittled behavior of this particular sample.

4. Conclusions

Confocal laser scanning microscopy is shown to be an effective tool for qualitative assessment of fracture surfaces from which quantitative measures can be derived. We defined a Real-to-Projected Area (RPA) metric/ratio based on the CLSM data and demonstrated that it can be used to quantitively describe fracture surface of engineering materials such as Mg, Ti, and Ni alloys. Values of RPA were established to be in a range of 40–80 pct for fatigue fracture surfaces and 90–140 pct for monotonic tension fracture surfaces with larger differences for more ductile materials. These ranges can be used reliably to determine a fracture type in similar materials when type of loading (fatigue vs monotonic) is unknown. We found that RPA is not sufficiently sensitive to stress or strain amplitudes for fracture surfaces of tested specimens in fatigue. Therefore, specimens tested in LCF or HCF were considered as a single group for estimating RPA. We used CLSM to characterize the presence of critical defects i.e. inclusions in Mg LPSO 5% alloy. Such qualitative observations were supported by quantification using RPA. Therefore, the quantitative methodology can be of importance in fractography for not only to distinguish monotonic versus fatigue fracture but also to determine the presence of critical defects in the microstructure. Finally, the quantitative measure successfully identified an invalid LCF tests for the Mg LPSP 50% alloy.

Data availability

The raw/processed data required to reproduce these findings cannot be shared at this time due to technical or time limitations.

Declaration of Competing Interest

The authors declare that they have no known competing financial interests or personal relationships that could have appeared to influence the work reported in this paper.

Data availability

Data will be made available on request.

Acknowledgements

This research was sponsored by the U.S. National Science Foundation and was accomplished under the CAREER grant no. CMMI-1650641.

Appendix

This appendix presents geometry of LCF and HCF test samples (Fig. A1) and selected 3D height maps of fracture surfaces (Fig. A2).

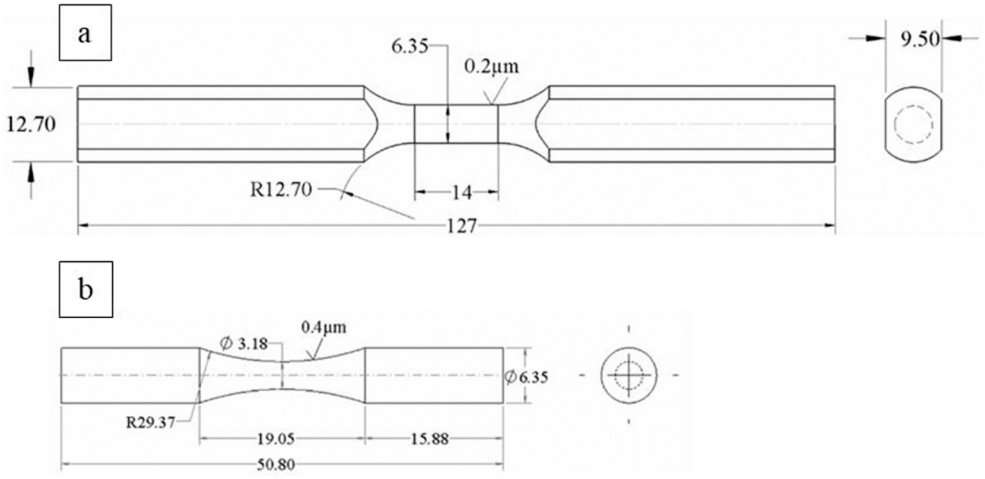

Fig. A1. Geometry of test specimens for (a) low-cycle fatigue and (b) high-cycle fatigue.

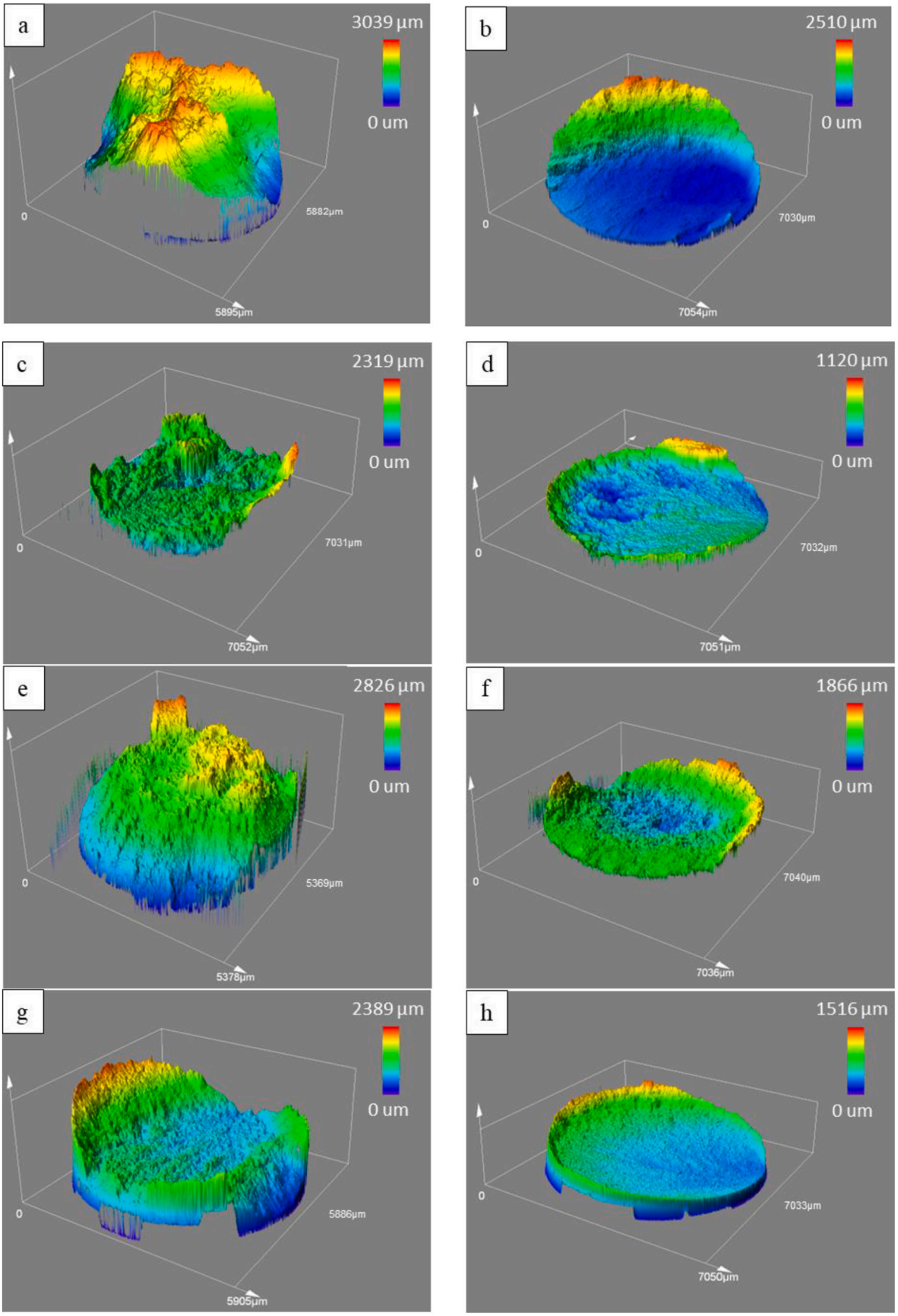

Fig. A2. 3D height maps of fracture surfaces for: (a,b) Mg LPSO 5%, (c,d) Mg LPSO 50%, (e,f) Inconel 718, (g,h) WE43, (i,j) Ti64 non-HT, and (k) Ti64 HT. (a,c,e,g,i, k) are from monotonic tension tests and (b,d,f,h,j) are from LCF tests at a strain amplitude of 1.2%.

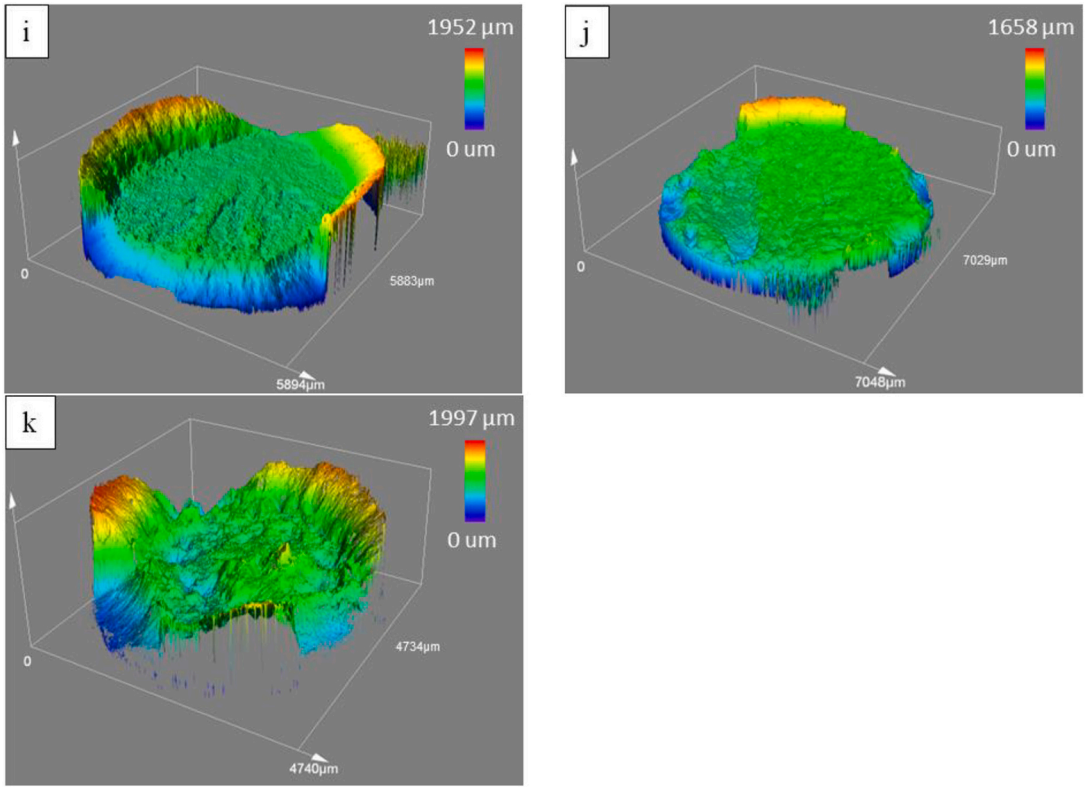

Fig. A2. (*continued*).

References

[1] S. Ramakrishna, et al., Materials informatics, J. Intell. Manuf. (2019), https://doi.org/10.1007/s10845-018-1392-0.

[2] D.L. McDowell, R.A. Lesar, The need for microstructure informatics in process-structure-property relations, MRS Bull. (2016), https://doi.org/10.1557/mrs.2016.163.

[3] M. Jahedi, E. Ardjmand, M. Knezevic, Microstructure metrics for quantitative assessment of particle size and dispersion: application to metal-matrix composites, Powder Technol. 311 (2017) 226–238, https://doi.org/10.1016/j.powtec.2017.01.093.

[4] A. Eghtesad, T.J. Barrett, M. Knezevic, Compact reconstruction of orientation distributions using generalized spherical harmonics to advance large-scale crystal plasticity modeling: Verification using cubic, hexagonal, and orthorhombic polycrystals, Acta Mater. 155 (2018) 418–432, https://doi.org/10.1016/j.actamat.2018.06.017.

[5] T.J. Barrett, et al., A generalized spherical harmonics-based procedure for the interpolation of partial datasets of orientation distributions to enable crystal mechanics-based simulations, Materialia 6 (2019), 100328, https://doi.org/10.1016/j.mtla.2019.100328.

[6] M. Knezevic, N.W. Landry, Procedures for reducing large datasets of crystal orientations using generalized spherical harmonics, Mech. Mater. 88 (0) (2015) 73–86, https://doi.org/10.1016/j.mechmat.2015.04.014.

[7] S.R. Kalidindi, M. Knezevic, S. Niezgoda, J. Shaffer, Representation of the orientation distribution function and computation of first-order elastic properties closures using discrete Fourier transforms, Acta Mater. 57 (13) (2009) 3916–3923, https://doi.org/10.1016/j.actamat.2009.04.055.

[8] M. Zecevic, R.J. McCabe, M. Knezevic, A new implementation of the spectral crystal plasticity framework in implicit finite elements, Mech. Mater. 84 (0) (2015) 114–126, https://doi.org/10.1016/j.mechmat.2015.01.018.

[9] J.B. Shaffer, M. Knezevic, S.R. Kalidindi, Building texture evolution networks for deformation processing of polycrystalline fcc metals using spectral approaches: Applications to process design for targeted performance, Int. J. Plast. 26 (8) (2010) 1183–1194 [Online]. Available, http://www.sciencedirect.com/science/article/pii/S0749641910000586.

[10] X. Wu, G. Proust, M. Knezevic, S.R. Kalidindi, Elastic-plastic property closures for hexagonal close-packed polycrystalline metals using first-order bounding theories, Acta Mater. 55 (8) (2007) 2729–2737 [Online]. Available, http://www.sciencedirect.com/science/article/B6TW8-4N2D69T-2/2/f94ae3c909cd0c26fab24911116eb286.

[11] F. Roters, P. Eisenlohr, L. Hantcherli, D.D. Tjahjanto, T.R. Bieler, D. Raabe, Overview of constitutive laws, kinematics, homogenization and multiscale methods in crystal plasticity finite-element modeling: Theory, experiments, applications, Acta Mater. 58 (4) (2010) 1152–1211 [Online]. Available, http://www.sciencedirect.com/science/article/pii/S1359645409007617.

[12] M. Knezevic, B. Drach, M. Ardeljan, I.J. Beyerlein, Three dimensional predictions of grain scale plasticity and grain boundaries using crystal plasticity finite element models, Comput. Methods Appl. Mech. Eng. 277 (0) (2014) 239–259, https://doi.org/10.1016/j.cma.2014.05.003.

[13] T.J. Barrett, D.J. Savage, M. Ardeljan, M. Knezevic, An automated procedure for geometry creation and finite element mesh generation: Application to explicit grain structure models and machining distortion, Comput. Mater. Sci. 141 (Supplement C) (2018) 269–281, https://doi.org/10.1016/j.commatsci.2017.09.048.

[14] T.J. Barrett, M. Knezevic, Deep drawing simulations using the finite element method embedding a multi-level crystal plasticity constitutive law: Experimental verification and sensitivity analysis, Comput. Methods Appl. Mech. Eng. 354 (2019) 245–270, https://doi.org/10.1016/j.cma.2019.05.035.

[15] Z. Feng, M. Zecevic, M. Knezevic, Stress-assisted (γ→α') and strain-induced (γ→ε→α') phase transformation kinetics laws implemented in a crystal plasticity model for predicting strain path sensitive deformation of austenitic steels, Int. J. Plast. 136 (2021), 102807, https://doi.org/10.1016/j.ijplas.2020.102807.

[16] M. Zecevic, M.V. Upadhyay, E. Polatidis, T. Panzner, H. Van Swygenhoven, M. Knezevic, A crystallographic extension to the Olson-Cohen model for predicting strain path dependence of martensitic transformation, Acta Mater. 166 (2019) 386–401, https://doi.org/10.1016/j.actamat.2018.12.060.

[17] M. Zecevic, I.J. Beyerlein, M. Knezevic, Coupling elasto-plastic self-consistent crystal plasticity and implicit finite elements: applications to compression, cyclic tension-compression, and bending to large strains, Int. J. Plast. 93 (2017) 187–211, https://doi.org/10.1016/j.ijplas.2016.07.016.

[18] M. Zecevic, M. Knezevic, A new visco-plastic self-consistent formulation implicit in dislocation-based hardening within implicit finite elements: application to high strain rate and impact deformation of tantalum, Comput. Methods Appl. Mech. Eng. 341 (2018) 888–916, https://doi.org/10.1016/j.cma.2018.07.027.

[19] A.M. Cantara, M. Zecevic, A. Eghtesad, C.M. Poulin, M. Knezevic, Predicting elastic anisotropy of dual-phase steels based on crystal mechanics and microstructure, Int. J. Mech. Sci. 151 (2019), https://doi.org/10.1016/j.ijmecsci.2018.12.021.

[20] M. Knezevic, M. Zecevic, I.J. Beyerlein, R.A. Lebensohn, A numerical procedure enabling accurate descriptions of strain rate-sensitive flow of polycrystals within crystal visco-plasticity theory, Comput. Methods Appl. Mech. Eng. 308 (2016) 468–482, https://doi.org/10.1016/j.cma.2016.05.025.

[21] J.D.G. Sumpter, J.S. Kent, Prediction of ship brittle fracture casualty rates by a probabilistic method, Mar. Struct. (2004), https://doi.org/10.1016/j.marstruc.2005.03.003.

[22] T.L. Anderson, Fracture Mechanics: Fundamentals and Applications, Fourth edition, 2017.

[23] S. Suresh, Fatigue of Materials, 1998, https://doi.org/10.1017/cbo9780511806575.

[24] M. Zecevic, Y.P. Korkolis, T. Kuwabara, M. Knezevic, Dual-phase steel sheets under cyclic tension–compression to large strains: Experiments and crystal plasticity

modeling, J. Mech. Phys. Solids 96 (2016) 65–87, https://doi.org/10.1016/j.jmps.2016.07.003.
[25] H. Zare, M. Jahedi, M.R. Toroghinejad, M. Meratian, M. Knezevic, Microstructure and mechanical properties of carbon nanotubes reinforced aluminum matrix composites synthesized via equal-channel angular pressing, Mater. Sci. Eng. A 670 (2016) 205–216, https://doi.org/10.1016/j.msea.2016.06.027.
[26] ASM International, ASM handbook-Vol 19: fatigue and fracture, in: Igarss, 2014, p. 2014.
[27] E. Merson, V. Danilov, D. Merson, A. Vinogradov, Confocal laser scanning microscopy: the technique for quantitative fractographic analysis, Eng. Fract. Mech. (2017), https://doi.org/10.1016/j.engfracmech.2017.04.026.
[28] M. Martínez-Corral, G. Saavedra, Chapter 1 the resolution challenge in 3D optical microscopy, Prog. Opt. (2009), https://doi.org/10.1016/S0079-6638(08)00201-1.
[29] F. Janoos, K. Mosaliganti, X. Xu, R. Machiraju, K. Huang, S.T.C. Wong, Robust 3D reconstruction and identification of dendritic spines from optical microscopy imaging, Med. Image Anal. (2009), https://doi.org/10.1016/j.media.2008.06.019.
[30] H. Ostadi, K. Jiang, P.D. Prewett, Characterisation of FIB milling yield of metals by SEM stereo imaging technique, Microelectron. Eng. (2009), https://doi.org/10.1016/j.mee.2009.01.056.
[31] S. Diamond, S. Mindess, SEM investigations of fracture surfaces using stereo pairs: III fracture surfaces of mortars, Cem. Concr. Res. (1994), https://doi.org/10.1016/0008-8846(94)90038-8.
[32] A.J. Lacey, N.A. Thacker, S. Crossley, R.B. Yates, A multi-stage approach to the dense estimation of disparity from stereo SEM images, Image Vis. Comput. (1998), https://doi.org/10.1016/s0262-8856(97)00068-1.
[33] M. Alff, Automatic evaluation of surface topography by cross-correlation of SEM stereo pair images, Ultramicroscopy (1986), https://doi.org/10.1016/0304-3991(86)90128-2.
[34] D.B. Hovis, A.H. Heuer, The use of laser scanning confocal microscopy (LSCM) in materials science, J. Microsc. (2010), https://doi.org/10.1111/j.1365-2818.2010.03399.x.
[35] D.N. Hanlon, I. Todd, E. Peekstok, W.M. Rainforth, S. van der Zwaag, The application of laser scanning confocal microscopy to tribological research, Wear (2001), https://doi.org/10.1016/S0043-1648(01)00727-X.
[36] B.V.R. Tata, B. Raj, Confocal laser scanning microscopy: applications in material science and technology, Bull. Mater. Sci. (1998), https://doi.org/10.1007/BF02744951.
[37] R. Leiva-Garca, J. Garca-Antn, M. Jos, Application of confocal laser scanning microscopy to the in-situ and ex-situ study of corrosion processes, Laser Scann. Theory Applicat. (2011), https://doi.org/10.5772/16161.
[38] E. Merson, A.V. Kudrya, V.A. Trachenko, D. Merson, V. Danilov, A. Vinogradov, Quantitative characterization of cleavage and hydrogen-assisted quasi-cleavage fracture surfaces with the use of confocal laser scanning microscopy, Mater. Sci. Eng. A (2016), https://doi.org/10.1016/j.msea.2016.04.023.
[39] E. Merson, A.V. Kudrya, V.A. Trachenko, D. Merson, V. Danilov, A. Vinogradov, The Use of Confocal Laser Scanning Microscopy for the 3D Quantitative Characterization of Fracture Surfaces and Cleavage Facets, 2016, https://doi.org/10.1016/j.prostr.2016.06.069.
[40] M. Knezevic, S.R. Kalidindi, Fast computation of first-order elastic-plastic closures for polycrystalline cubic-orthorhombic microstructures, Comput. Mater. Sci. 39 (3) (2007) 643–648 [Online]. Available, http://www.sciencedirect.com/science/article/B6TWM-4M93P5N-2/2/a22c7254959580013e0dd8b142d5814c.
[41] C.M. Poulin, S.C. Vogel, Y.P. Korkolis, B.L. Kinsey, M. Knezevic, Experimental studies into the role of cyclic bending during stretching of dual-phase steel sheets, Int. J. Mater. Form. 13 (3) (2020) 393–408, https://doi.org/10.1007/s12289-019-01530-2.
[42] M. Knezevic, C.M. Poulin, X. Zheng, S. Zheng, I.J. Beyerlein, Strengthening of alloy AA6022-T4 by continuous bending under tension, Mater. Sci. Eng. A 758 (2019) 47–55, https://doi.org/10.1016/j.msea.2019.04.109.
[43] C.M. Poulin, T.J. Barrett, M. Knezevic, Inferring post-necking strain hardening behavior of sheets by a combination of continuous bending under tension testing and finite element modeling, Exp. Mech. 60 (4) (2020) 459–473, https://doi.org/10.1007/s11340-019-00577-1.
[44] M. Jahedi, M.H. Paydar, M. Knezevic, Enhanced microstructural homogeneity in metal-matrix composites developed under high-pressure-double-torsion, Mater. Charact. 104 (0) (2015) 92–100, https://doi.org/10.1016/j.matchar.2015.04.012.
[45] H. Zare, M. Jahedi, M.R. Toroghinejad, M. Meratian, M. Knezevic, Compressive, shear, and fracture behavior of CNT reinforced Al matrix composites manufactured by severe plastic deformation, Mater. Des. 106 (2016) 112–119, https://doi.org/10.1016/j.matdes.2016.05.109.
[46] E.D. Merson, V.A. Danilov, M.L. Linderov, P.N. Myagkikh, D.L. Merson, A. Vinogradov, Assessing Fracture Surface Ductility by Confocal Laser Scanning Microscopy, 2018, https://doi.org/10.1016/j.prostr.2018.12.149.
[47] J. Wang, et al., Understanding the high strength and good ductility in LPSO-containing Mg Alloy using synchrotron X-ray diffraction, Metall. Mater. Trans. A Phys. Metall. Mater. Sci. (2018), https://doi.org/10.1007/s11661-018-4881-z.
[48] S. Gribbin, S. Ghorbanpour, N.C. Ferreri, J. Bicknell, I. Tsukrov, M. Knezevic, Role of grain structure, grain boundaries, crystallographic texture, precipitates, and porosity on fatigue behavior of Inconel 718 at room and elevated temperatures, Mater. Charact. 149 (2019) 184–197, https://doi.org/10.1016/j.matchar.2019.01.028.
[49] S. Ghorbanpour, B.A. McWilliams, M. Knezevic, Effect of hot working and aging heat treatments on monotonic, cyclic, and fatigue behavior of WE43 magnesium alloy, Mater. Sci. Eng. A 747 (2019) 27–41, https://doi.org/10.1016/j.msea.2019.01.056.
[50] I.A. Riyad, et al., Modeling the role of local crystallographic correlations in microstructures of Ti-6Al-4V using a correlated structure visco-plastic self-consistent polycrystal plasticity formulation, Acta Mater. 203 (2021), 116502, https://doi.org/10.1016/j.actamat.2020.116502.
[51] M. Knezevic, et al., Thermo-hydrogen refinement of microstructure to improve mechanical properties of Ti–6Al–4V fabricated via laser powder bed fusion, Mater. Sci. Eng. A 809 (2021), 140980, https://doi.org/10.1016/j.msea.2021.140980.
[52] S. Ghorbanpour, B.A. McWilliams, M. Knezevic, Low-cycle fatigue behavior of rolled WE43-T5 magnesium alloy, Fatigue Fract. Eng. Mater. Struct. 42 (6) (2019) 1357–1372, https://doi.org/10.1111/ffe.12992.
[53] W.G. Feather, et al., Mechanical response, twinning, and texture evolution of WE43 magnesium-rare earth alloy as a function of strain rate: experiments and multi-level crystal plasticity modeling, Int. J. Plast. 120 (2019) 180–204, https://doi.org/10.1016/j.ijplas.2019.04.019.
[54] M. Jahedi, B.A. McWilliams, P. Moy, M. Knezevic, Deformation twinning in rolled WE43-T5 rare earth magnesium alloy: Influence on strain hardening and texture evolution, Acta Mater. 131 (2017) 221–232, https://doi.org/10.1016/j.actamat.2017.03.075.
[55] M. Jahedi, B.A. McWilliams, F.R. Kellogg, I.J. Beyerlein, M. Knezevic, Rate and temperature dependent deformation behavior of as-cast WE43 magnesium-rare earth alloy manufactured by direct-chill casting, Mater. Sci. Eng. A 712 (2018) 50–64, https://doi.org/10.1016/j.msea.2017.11.092.
[56] M. Jahedi, B.A. McWilliams, M. Knezevic, Deformation and fracture mechanisms in WE43 magnesium-rare earth alloy fabricated by direct-chill casting and rolling, Mater. Sci. Eng. A 726 (2018) 194–207, https://doi.org/10.1016/j.msea.2018.04.090.
[57] S. Ghorbanpour, et al., A crystal plasticity model incorporating the effects of precipitates in superalloys: application to tensile, compressive, and cyclic deformation of Inconel 718, Int. J. Plast. 99 (Supplement C) (2017) 162–185, https://doi.org/10.1016/j.ijplas.2017.09.006.
[58] S. Ghorbanpour, et al., Experimental characterization and crystal plasticity modeling of anisotropy, tension-compression asymmetry, and texture evolution of additively manufactured Inconel 718 at room and elevated temperatures, Int. J. Plast. 125 (2020) 63–79, https://doi.org/10.1016/j.ijplas.2019.09.002.
[59] D.H. Smith, et al., Microstructure and mechanical behavior of direct metal laser sintered Inconel alloy 718, Mater. Charact. 113 (2016) 1–9, https://doi.org/10.1016/j.matchar.2016.01.003.
[60] S. Gribbin, J. Bicknell, L. Jorgensen, I. Tsukrov, M. Knezevic, Low cycle fatigue behavior of direct metal laser sintered Inconel alloy 718, Int. J. Fatigue 93 (Part 1) (2016) 156–167, https://doi.org/10.1016/j.ijfatigue.2016.08.019.
[61] N.C. Ferreri, et al., Effects of build orientation and heat treatment on the evolution of microstructure and mechanical properties of alloy Mar-M-509 fabricated via laser powder bed fusion, Int. J. Plast. 121 (2019) 116–133, https://doi.org/10.1016/j.ijplas.2019.06.002.